

PHR J1724-3859: A Bipolar Planetary Nebula in Open Cluster Trumpler 25*

VASILIKI FRAGKOU ¹, QUENTIN A. PARKER ² AND DENISE R. GONÇALVES ¹

¹*Universidade Federal do Rio de Janeiro, Observatório do Valongo, Ladeira do Pedro Antônio, 43, Saúde CEP 20080-090 Rio de Janeiro, R.J, Brazil*

²*The Laboratory for Space Research, The University of Hong Kong, Cyberport 4, Pokfulam, Hong Kong*

ABSTRACT

Planetary nebulae (PNe) studies are essential for understanding late stellar evolution of low-to-intermediate mass stars. PNe in open clusters (OC) are rare but valuable since their study directly links their properties to those of their progenitors, something that cannot be achieved for field PNe. Here, we report the identification of one more OC-PN association to add to the small sample of, now, five pairs. The physical properties of the host cluster, PN and its central star (CSPN) have been explored using high and intermediate-resolution spectral and deep photometric data. The close agreement of the radial velocities of the PN and host cluster, together with concordance of reddening and distance, show that the PN PHR J1724-3859 is highly likely to be physically associated with the OC Trumpler 25. Deep photometric data allowed clear identification of the CSPN. We find a CSPN effective temperature of around 250 kK and a nebular kinematic age of 23 kyrs, both at the extreme end, like the other members of this small class. The progenitor and final CSPN masses have been estimated to be $5.12^{+0.16}_{-0.15} M_{\odot}$ and $0.95 \pm 0.12 M_{\odot}$ respectively. These latest results agree with the emerging trend for our other OC-PNe, falling below, but approximately parallel to, the latest initial-to-final-mass relation estimates derived from cluster white dwarfs and has important implications for stellar evolution models. All OC-PNe also possess some other common properties (e.g. all are Type-I PNe and bipolars) to be explored in future studies.

Keywords: Planetary Nebulae(1249) — Open clusters(1160) — Spectroscopy(1558) — Photometry(1234)

1. INTRODUCTION

Planetary nebulae (PNe) are the final stages of evolution of low-to-intermediate mass stars (1-8 M_{\odot}). They consist of the remnant core - on the way to becoming or already a white dwarf (WD) and the previously ejected material comprising gas and dust. As such, study of the Galactic PN population provides valuable information on the chemical enrichment process in our Galaxy, late stage stellar evolution processes, Galactic kinematics (using PNe as point probes) and the role of binary stars in ejecta shaping (PN morphology).

A notable problem in PNe studies is linking PN properties to the properties of their main sequence (MS) progenitor stars. This issue can be more easily evaluated for PNe that are physical members of star clusters. PN properties can be estimated from spectrophotometric observations, while the progenitor properties (since cluster stars share some common physical characteristics) can be determined from cluster colour-magnitude diagrams (CMD) and theoretical isochrones (A. Bressan et al. 2012). Unfortunately, the sample of identified PNe in Galactic star clusters is very small, with only four confirmed in globular clusters (F. G. Pease 1928; F. C. Gillett et al. 1989; G. H. Jacoby et al. 1997) and four in open clusters (Q. A. Parker et al. 2011; V. Fragkou et al. 2019a,b, 2022, 2025). Any new cluster-PN identification and confirmation is a valuable datum to add to this rare sample. such confirmations require consistent and precise cluster and PN radial velocities to within tight errors/dispersions. Accurate cluster radial veloci-

Corresponding author: Quentin A. Parker, Vasiliki Fragkou
quentinp@hku.hk, vfragkou@ov.ufrj.br

* based on observations made with the Southern African Large Telescope (SALT), the ESO Vary Large Telescope (VLT) and the Gemini telescope.

ties can often be determined from Gaia data of cluster stars (Gaia Collaboration et al. 2022), while for the PN, high resolution spectral data are required, unless their faint, low luminosity central stars are identified and fall within Gaia’s reach.

In Section 2 and Section 3 we briefly describe the open cluster and PN. In Section 4 we describe our observations, while in Section 5 we introduce our results. Finally, in Section 6 we discuss our findings and in Section 7 we state our conclusions.

2. THE HOST CLUSTER TRUMPLER 25

The open cluster (OC) Trumpler 25 is a relatively well studied OC of medium richness (S. van den Bergh & G. L. Hagen 1975) first detected by R. J. Trumpler (1930) and is approximately 9.5 arcmin in diameter. The cluster physical parameters have been explored by multiple authors in the literature: (A. F. Seleznev et al. 2010; N. V. Kharchenko et al. 2013; W. S. Dias et al. 2014; H. Monteiro et al. 2017; L. Sampeiro et al. 2017; C. Soubiran et al. 2018; T. Cantat-Gaudin et al. 2018; L. Liu & X. Pang 2019; T. Cantat-Gaudin et al. 2020; N. Sánchez et al. 2020; Y. Tarricq et al. 2021; C. J. Hao et al. 2021; W. S. Dias et al. 2021; C. J. Hao et al. 2022; Z. Li et al. 2022; D. Liu et al. 2023; E. L. Hunt & S. Reffert 2024; L. Cavallo et al. 2024; M. S. Angelo et al. 2025). The weighted average of the reported literature cluster parameters gives a cluster systemic radial velocity of $-26.2 \pm 2.3 \text{ km s}^{-1}$ if we exclude the radial velocities estimated by D. Liu et al. (2023) and C. J. Hao et al. (2021) who use older catalogues for cluster members and ≤ 5 stars. Using the values found by the same authors, we also find proper motions of $\text{pmRA} = 0.3 \pm 0.4 \text{ mas yr}^{-1}$ and $\text{pmDEC} = -2.1 \pm 0.3 \text{ mas yr}^{-1}$, a cluster mean parallax of $0.46 \pm 0.05 \text{ mas}$, a distance of $1.8 \pm 0.1 \text{ kpc}$, a reddening $E(B - V) = 0.89 \pm 0.04$ (implying an extinction of $A_v = 2.75 \pm 0.13$ using the J. A. Cardelli et al. (1989) extinction law with $R_v=3.1$), an age of $118 \pm 21 \text{ Myr}$ and an iron abundance of $[\text{Fe}/\text{H}] = 0.28 \pm 0.04$, which implies a metallicity of $Z = 0.029 \pm 0.003$ for $Z_\odot = 0.0152$ (A. Bressan et al. 2012). For literature parameter values with no assigned errors, we assume an error of 20 %.

3. THE OC PN CANDIDATE: FAINT BIPOLAR PN PHR J1724-3859

The low surface brightness, extended, bipolar, high excitation PN PHR J1724-3859 was first discovered by visual inspection of the photographic SuperCOSMOS $\text{H}\alpha$ Survey (SHS) data (Q. A. Parker et al. 2005) by Parker (private communication) and reported in the Macquarie/AAO/Strasbourg $\text{H}\alpha$ Planetary Nebula (MASH)

catalogue (Q. A. Parker et al. 2006) and subsequently in the Hong Kong/AAO/Strasbourg $\text{H}\alpha$ planetary nebula (HASH) database (Q. A. Parker et al. 2016) where it has HASH ID#3064. It was considered by us early as an excellent candidate member of OC Trumpler 25 due to its close projection on the main cluster area, (see Figure 1) and also briefly explored by V. Fragkou (2019). It has an apparent size of $152 \times 96 \text{ arcsec}^2$ (Q. A. Parker et al. 2006). Preliminary nebular spectra taken in May, 2000 on the SAAO 1.9 m telescope (PI: Parker) show nitrogen enrichments with the observed $\text{H}\alpha/[\text{NII}]$ line ratio being ~ 12 , indicating Type I chemistry (M. Peimbert & S. Torres-Peimbert 1983). The $[\text{OIII}]$ emission was very weak, likely due to extinction (Q. A. Parker et al. 2006; V. Fragkou 2019). Its integrated $\text{H}\alpha$ flux has been estimated to be $\log F(\text{H}\alpha) = -12.17 \text{ mW/m}^2$ (D. J. Frew et al. 2013). Recently, I. González-Santamaría et al. (2021) reported the detection of the central star (CSPN) of PHR J1724-3859 using Gaia EDR3 data (Gaia Collaboration et al. 2022). However, as we show below, this is almost certainly a false identification. Many true CSPN are simply too faint to be detected with Gaia where the level of false identification of Gaia CSPN reported in I. González-Santamaría et al. (2021) is estimated to be as high as $\sim 20\%$ (Q. A. Parker et al. 2022). The PN’s estimated geometric centre position lies only ~ 90 arcseconds North from Trumpler 25’s reported centre (see Figure 1). This is well within the cluster’s tidal radius of ~ 16.6 arcminutes from the physical estimate of 11.6 pc E. L. Hunt & S. Reffert (2024).

4. OBSERVATIONS

Archival narrow-band imaging data (SHS), together with the latest Gaia DR3 (Gaia Collaboration et al. 2022) cluster data were used for imaging and photometry. This was supplemented with our new, high-resolution echelle High Resolution Spectrograph (HRS) data from the 9.2 m South African Large Telescope (SALT) and also with IFU 8.2 m Gemini High-resolution Optical Spectrograph (GHOST) spectral data. We then obtained new, deep cluster photometry with the Focal Reducer and low dispersion Spectrograph (FORS2) mounted on the 8.2 m ESO Very Large Telescope (VLT). We further obtained FORS2 intermediate-resolution long-slit spectra. Combining all these data allowed us to derive new, key PN and cluster properties. The archival SHS data provided initial evidence indicating a likely association of the PN and cluster, while the Gaia DR3 data were used to derive the mean kinematic properties of the cluster (see Subsection 5.1) and establish high cluster membership probability supported by our new high-resolution data (see Subsection 5.2). The FORS2

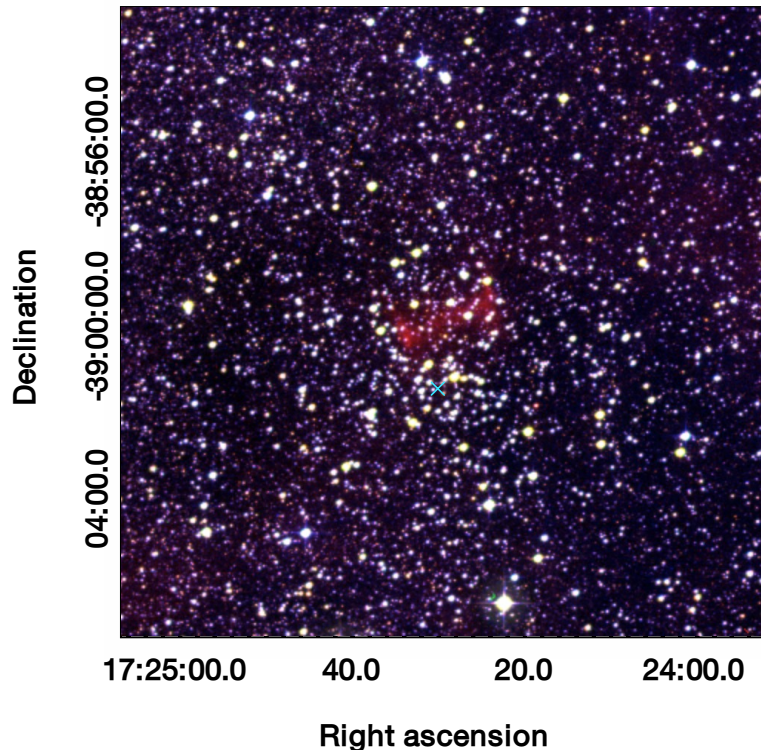


Figure 1. A 3-colour (R is $H\alpha$, G is short-red and B is blue) SHS image, 15×15 arcminutes in size, of the open cluster Trumpler 25 and PN PHR J1724-3859. North East is to top-left. The image is centred on the faint bipolar PN, clearly identified just 90 arcseconds North of the cluster’s reported equatorial coordinate centre of RA:17h24m30.70s and

imaging data have been used for the estimation of the cluster mean parameters and the identification of the CSPN (see Subsections 5.1, 5.3) and the FORS2 long-slit spectral data allowed a further examination of the nebular spectral properties (see Subsection 5.2).

The aforementioned data show that PN PHR J1724-3859 is highly likely a physical member of open cluster Trumpler 25. This evaluation is based on the PN and OC radial velocities being closely matched to $\leq 3 \text{ km s}^{-1}$, within the tight errors (a fundamental requirement), the distances of PN and cluster in excellent concordance, also to within the reasonable errors (another key condition), the reddenings being in close agreement, the PN physical size being plausible as a cluster member and the PN being situated well within the projected cluster tidal radius.

While each compatibility on its own is equivocal, taken together they present a compelling argument for true OC-PN association. Indeed, on comparing this example with the four other OC-PN pairs currently known, several shared properties, unusual for most PNe, are

also found. This further strengthens the arguments (see later).

4.1. *Intermediate-resolution ESO VLT FORS2 imaging and spectroscopy*

As a valuable supplement to our large-telescope high resolution spectroscopy from SALT and Gemini and to facilitate a more in-depth cluster and PN study, we had earlier collected deep photometric imaging and lower resolution spectroscopic data for the PN and cluster using the FORS2 imager and spectrograph on the Cassegrain focus of the ESO 8.2 m VLT UT1 telescope. Data were obtained under Program IDs 0103.D-0093(A) and 0103.D0093(B) for observations with the E2V (acquisition date: 31 May, 2019) and MIT (acquisition date: 02 June, 2019) detectors respectively.

4.1.1. *FORS2 photometric data*

For an independent study of the cluster physical parameters, and to robustly identify and then characterize the CSPN, we collected imaging data with the u-high, b-high, v-high, Bessel R ‘special’ and Bessel I filters with the FORS2 imager centred on the PN. These filter pass-

bands are effectively equivalent to the UBVRI Johnson-Cousins photometric system (M. S. Bessell 1990, 2005). The FORS2 imager on the VLT has two field of view options, selected via different collimators. In the case of our exposures with the u-high, b-high, v-high and Bessel R special filters, we used the standard resolution (SR) collimator with a field of view of 7.1×7.1 arcmin to sample as much of the cluster as possible in a single pointing, corresponding to pixel scales of $0.25''$ /pixel. In the case of our exposures using the Bessel I filter, we used the high resolution collimator. The u-high, b-high and v-high imaging filters were used to construct the cluster CMD and for CSPN identification. The Bessel R special and Bessel I filters were used for the further characterization of the CSPN. Both short and long exposures were acquired with each filter for the purpose of collecting reliable photometry of both bright and faint stellar sources in our field.

Observations with the u-high, b-high and v-high filters (centred on J2000 RA: 17h24m28.78s, DEC:-39°00'07.10") employed the E2V detector and standard resolution (SR) collimator and a low readout and a binning of 2×2 . Short exposures of 3 seconds were obtained with each of these three filters, while long exposures of 40, 15 and 40 seconds were acquired for the u-high, b-high and v-high filters respectively. In all cases the seeing was equal or better than 0.7 arcsec.

The MIT detector was used for observations with the Bessel R 'special' and Bessel I filters (centred on J2000 RA: 17h24m29.23s, DEC:-39°00'10.20"). We selected a low readout, and the standard resolution (SR) collimator for the Bessel R special observations and the high resolution (HR) collimator for the Bessel I observations, plus a binning of 2×2 and 1×1 for acquisitions with the Bessel R special and Bessel I filters respectively. A 5 and 3×120 sec short and long exposures were acquired with the Bessel R special filter, while a 10 and 5×120 sec exposures were acquired with the Bessel I filter. The seeing during these observations was around 1 arcsec.

All imaging data were reduced and processed with EsoReflex (W. Freudling et al. 2013), while the source extraction and photometry across Trumpler 25 was done with SExtractor within EsoReflex using mag_auto and the corresponding parameter files for FORS2 (fors2_stetson.sex, fors.param, fors.conv and fors.nnw). Consequently, the data were corrected for atmospheric extinction and colour term correction was applied. Zero-points, extinction coefficients and colour terms for each of our filters and CCD chips (FORS2 consists of two separate CCD chips that observe simultaneously) were

obtained from the FORS2 database³ for the time period of our observations. Since this information is not available for the u-high filter, u-high data were calibrated by cross-correlation with the A. Pickles & É. Depagne (2010) U magnitudes. The data were processed and calibrated separately for each FORS2 CCD chip, long (Bessel R special and Bessel I long exposures were combined) and short exposures. Calibrated data from long and short exposures in each filter were selected accordingly, in order to exclude saturated stars, and then combined. This resulted in a source catalogue that contains the maximum possible stellar magnitude range. Finally, the data from both CCD chips for each filter were combined.

4.1.2. FORS2 spectroscopic data

PN long-slit medium to low spectral data were acquired with the 1200B+97 (E2V detector, $R \approx 1420$) and 600RI+19 (MIT detector, $R \approx 1000$) grisms of FORS2. These covered the blue (3660-5110 Å with central $\lambda = 4350$ Å) and red (5120-8450 Å with central $\lambda = 6780$ Å) parts of the optical spectrum respectively. In both cases we used the SR collimator, a low readout and a binning of 2×2 . The slit length is 523 arcsec while a 1 arcsec slit width was selected. Acquisitions with the 1200B+97 (J2000 RA:17h24m28.78d, DEC:-39°00'07.10") and 600RI+19 (J2000 RA:17h24m29.2s, DEC:-39°00'10.20") grisms have a slit position angle of 65° and 68° ($N=0^\circ$, $E=90^\circ$) respectively, moderately inclined relative to the nebular bipolar axis, with an angle of about 65° . The exposure times were 3×900 seconds with the 1200B+97 grism and 3×600 seconds with the 600RI+19 grism. For the flux calibration of our data, we additionally observed the spectrophotometric standard star LTT 3864 with both grisms.

The spectral data were reduced and processed with EsoReflex (W. Freudling et al. 2013) and standard IRAF techniques. The data from each CCD chip were processed and calibrated separately before being combined for further analysis. The nebula is very extended, covering almost the entire FORS2 field. Consequently, and combined with the complications added by the separate FORS2 CCD chips and the crowded field, there is no adequate background sky region available to subtract from our science spectra so the sky subtraction is problematic. This limitation particularly affects the Balmer lines, since these are very bright in the residual sky and cannot be sufficiently subtracted from our science spectra. At the lower spectral resolutions here all identified

³ http://archive.eso.org/bin/qc1.cgi?action=qc1_browse.table&table=fors2_photometry

Balmer lines suffer from over-subtraction. These data were taken to cover a wide optical wavelength range to enable detection of as many PN emission lines as possible. The blue VLT FORS2 spectra (see Figure 5) clearly shows the [OIII], $H\beta$ and, for the first time, the high excitation He II line, enabling its identification as a high excitation PN. Any precise Balmer line ratios derived from analysis of these data should be taken with caution and as upper limits. The full log of our observations is presented in Table 1).

4.2. High-resolution spectra from SALT and Gemini telescopes

For determining the precise systemic radial velocity for PN PHR J1724-3859 we obtained high-resolution spectra across selected, representative parts of the PN using the HRS spectrograph on SALT, a 9.2 m telescope in Sutherland, South Africa and the GHOST spectrograph on the 8.2 m Gemini telescope in Chile. To estimate a precise PN radial velocity it is important to calculate its value across multiple symmetrically selected PN pointings to account for the internal gas motions (typical PNe expansion velocities are $\sim 25 - 30 \text{ km s}^{-1}$).

The SALT HRS is a high-resolution dual-beam echelle spectrograph capable of simultaneously acquiring a science and a sky frame in the same exposure. The dual beam covers wavelengths $3700\text{-}5500\text{\AA}$ in the blue and $5500\text{-}8900\text{\AA}$ in the red with a field of view of 2.23 arcsec diameter. Our data were obtained with director’s discretionary time under program: 2019-1-DDT-002 on the 3rd of June, 2019 in the echelle low-resolution mode with a resolution $R \approx 14000$. The binning was set to 1×1 , the gain to low while the pixel scale is 0.042 \AA/pixel . The seeing during our observations was 1.9 arcsec . We acquired two 900 sec exposures, one for each PN bipolar lobe. Due to the nebula extent, the corresponding sky frames are actually additional PN exposures, thus giving four PN pointings labelled ha, hb, hc and hd (see Figure 2). The data have been processed with the standard PySALT/PyHRS⁴ (S. M. Crawford et al. 2010, 2016) pipeline.

We also obtained high-resolution spectral data for six additional PN pointings using the GHOST spectrograph on the 8.2 m Gemini telescope under program: GS-2024A-Q-232 in June 2024 to further refine the velocities. We opted for the dual-IFU (integral field unit) standard-resolution configuration, allowing the observation of two separate PN pointings simultaneously. GHOST IFU’s have a field of view of $1.2 \times 1.2 \text{ arcsec}^2$, covering a wavelength range from 3830 to 10000\AA , us-

ing separate detectors for the blue and the red arm. GHOST’s resolution in the standard-resolution mode is $R = 56000$, allowing a radial velocity precision down to 1 km s^{-1} . We selected a CCD binning of 1×2 and a slow readout, while the pixel size in the spatial direction is 0.4 arcsec .

Four $3 \times 508 \text{ sec}$ exposures allowed the acquisition of spectra in six separate PN pointings (ga-gf), plus two sky pointings (gc_sky, gd_sky) for the background subtraction (see Figure 2). All our pointings were carefully selected in areas free of stars to avoid any possible stellar contamination in our PN spectra. Pointings ga-gf (observed on the 3rd of July, 2024), gb-ge (observed on the 1st of June, 2024), gd-gd_sky (observed on the 2nd of July, 2024) and gc-gc_sky (observed on the 3rd of July, 2024) were observed simultaneously. The sky pointing gd_sky was used for the sky subtraction of PN pointings ga, gb and gd, while the sky pointing gc_sky was used for the sky subtraction of PN pointings gc, ge and gf. All sky GHOST pointings were observed more than a month after the acquisition of the data for PN pointings gb and ge due to scheduling issues. The sky subtraction for these pointings is therefore not optimal, but still sufficient for our purposes. The seeing during our June and July observations was ≈ 0.8 and 0.7 arcsec respectively. The airmass during all our observations was around 1.

For reducing our HRS and GHOST data we employed the PySALT/PyHRS and DRAGONS 3.20 pipelines respectively, and standard IRAF techniques. Standard thorium-argon arc lamps, acquired before and after the science exposures, were used for the wavelength calibration in each case. GHOST is primarily intended to observe point sources and our data have no continuum, thus DRAGONS cannot handle the 1-D spectra extraction automatically. For extracting the 1-D spectra we had to make some additional adjustments following V. Fragkou et al. (2025). Flux calibration was not applied since it is not required for our radial velocity purposes, while barycentric correction was turned on. The sky frames were subtracted from the science ones with the IRAF task IMAGES/IMARITH.

5. RESULTS

In this Section we present our results concerning both the PN PHR J1724-3859 and the cluster Trumpler 25. Our findings regarding the cluster Trumpler 25 are presented in Subsection 5.1, while in Subsections 5.2 and 5.3 we report our results about the PN PHR J1724-3859 and its CSPN, respectively.

5.1. Properties of open cluster Trumpler 25

Gaia DR3 (Gaia Collaboration et al. 2022) provides accurate kinematic data for a very large sample of

⁴ <http://pysalt.salt.ac.za/>

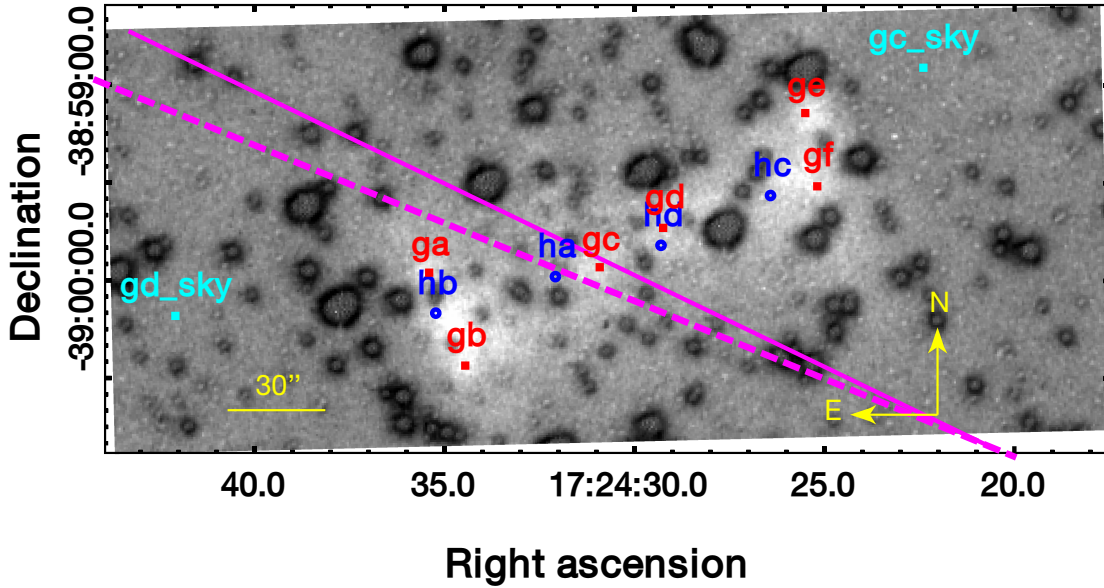


Figure 2. A quotient image from the SHS H α divided by the accompanying broad-band ‘short-red’ image of the PN PHR J1724-3859. The selected PN spectroscopic sampling points for HRS (in blue), GHOST (in red) and sky GHOST (in light blue), together with the FORS2 slits (continuous and dashed magenta lines for the blue and red grisms, respectively) are indicated. The size and shape of the point markings represent the respective HRS and GHOST fields of view which are very similar.

sources and has been used for the identification of open cluster members (M. G. J. van Groenigen et al. 2023). There are 550 stars assigned 100 % probability of being members of Trumpler 25 (M. G. J. van Groenigen et al. 2023). We use these for determining the cluster mean physical parameters. We find a mean pmRA= 0.315 ± 0.002 mas/yr, a mean pmDEC= -2.138 ± 0.002 mas/yr and a mean parallax of 0.414 ± 0.002 mas, which implies a cluster distance of 2417 ± 14 pc. Gaia DR3 radial velocities are available for 40 of these stars and from these we estimate a cluster weighted mean radial velocity of -25.5 km s $^{-1}$ with a weight standard deviation of 9.1 km s $^{-1}$ and a measurement uncertainty of 0.1 km s $^{-1}$. We use these cluster mean values for the remainder of our study. This observed dispersion, when OCs are usually expected to have an inherent velocity dispersion of $\sim 1 - 3$ km s $^{-1}$ is unusually high for an OC and may reflect a large binary fraction (see, A. M. Geller et al. 2010), explaining the 5 km s $^{-1}$ offset between the PN systemic velocity and the cluster average (see Section 5.2).

Our deep FORS2 photometry for stars with cluster membership probability of 100 % (M. G. J. van Groenigen et al. 2023) has been employed for the construction of the cluster CMD (see Figure 3) and the determination of the cluster physical parameters. Bessel R ‘special’ and Bessel I imaging data cannot be optimally paired

with the u-high, b-high and v-high data due to the different detectors and collimators used plus the different nights/seeing of their observations. As mentioned, u-high data were calibrated using literature photometry thus, they also cannot be optimally paired with data from other filters. For the aforementioned reasons, we use the more consistent b-high and v-high data for both the construction of the cluster CMD and the identification of the CSPN.

Padova theoretical isochrones (A. Bressan et al. 2012) were fitted to our cluster CMD to determine the cluster physical parameters. Keeping the precise Gaia cluster distance determined above fixed, we employed the ASteCA code (G. I. Perren et al. 2015) for determining the best fit isochrone and the remaining cluster physical parameters. We find that the cluster parameters for the isochrone (A. Bressan et al. 2012; Y. Chen et al. 2014; J. Tang et al. 2014; Y. Chen et al. 2015; P. Marigo et al. 2017; G. Pastorelli et al. 2019, 2020) that best fits our data are a cluster age of 112 ± 9 Myrs, a metal content of $[\text{Fe}/\text{H}] = 0.17 \pm 0.02$ (implying a metallicity of $Z = 0.023 \pm 0.001$ for $Z_{\odot} = 0.0152$ following A. Bressan et al. (2012)), a reddening of $E[\text{B}-\text{V}] = 0.85 \pm 0.01$ (implying an extinction of $A_v = 2.64 \pm 0.04$ using the J. A. Cardelli et al. (1989) extinction law with $R_v = 3.1$) and a differential reddening of $DR = 0.21 \pm 0.02$. In Figure 3 we show how the theoretical isochrones pro-

Table 1. The complete log of our observations.

ID	RA	DEC	Instrument	Mode	R ^a	Date	Exp. time (sec)	Seeing (")
ha	17:24:32	-38:59:59	HRS/SALT	low resolution ^b	14000	03/06/19	900	~1.9
hb	17:24:35	-39:00:10	HRS/SALT	low resolution	14000	03/06/19	900	~1.9
hc	17:24:26	-38:59:34	HRS/SALT	low resolution	14000	03/06/19	900	~1.9
hd	17:24:29	-38:59:49	HRS/SALT	low resolution	14000	03/06/19	900	~1.9
ga	17:24:35	-38:59:58	GHOST/Gemini	double IFU	56000 ^c	03/07/24	3×508	~0.7
gb	17:24:35	-39:00:26	GHOST/Gemini	double IFU	56000	01/06/24	3×508	~0.8
gc	17:24:31	-38:59:56	GHOST/Gemini	double IFU	56000	03/07/24	3×508	~0.7
gd	17:24:29	-38:59:44	GHOST/Gemini	double IFU	56000	02/07/24	3×508	~0.7
ge	17:24:26	-38:59:09	GHOST/Gemini	double IFU	56000	01/06/24	3×508	~0.8
gf	17:24:25	-38:59:31	GHOST/Gemini	double IFU	56000	03/07/24	3×508	~0.7
gc_sky	17:24:22	-38:58:55	GHOST/Gemini	double IFU	56000	03/07/24	3×508	~0.7
gd_sky	17:24:42	-39:00:11	GHOST/Gemini	double IFU	56000	02/07/24	3×508	~0.7
fors2blue	17:24:29	-39:00:07	FORS2/VLT	spec: E2V, 1200B+197	1420	31/05/19	3×900	~0.7
fors2red	17:24:29	-39:00:10	FORS2/VLT	spec: MIT, 600RI+19	1000	02/06/19	3×600	~1
fors2u	17:24:29	-39:00:07	FORS2/VLT	imag: E2V, u-high		31/05/19	3, 40	~0.7
fors2b	17:24:29	-39:00:07	FORS2/VLT	imag: E2V, b-high		31/05/19	3, 15	~0.7
fors2v	17:24:29	-39:00:07	FORS2/VLT	imag: E2V, v-high		31/05/19	3, 40	~0.7
fors2R	17:24:29	-39:00:10	FORS2/VLT	imag: MIT, Bessel R sp.		02/06/19	5, 3×120	~1
fors2I	17:24:29	-39:00:10	FORS2/VLT	imag: MIT, Bessel I		02/06/19	10, 5×120	~1

^aResolving power.

^bRefers to the instrument mode used, not to be confused with the actual resolution of the spectrograph.

^cThe GHOST radial velocity precision was measured from the obtained sky data to be equal to 0.04 km s⁻¹.

duced from using the previously calculated mean literature values (see Section 1, green isochrone) and the ASteCa code (brown isochrone) fit our FORS2 data for stars with cluster membership probability of 100 %. The two isochrones are very similar, but the one calculated with the ASteCa code presents a slightly better fit.

The ASteCa best fitted isochrone presents a turn-off (TO) point at B-V=0.685 and B=13.15 and, crucially, a TO mass of 4.88 M_{\odot} . Taking into consideration the time needed to leave the MS and pass through the Asymptotic Giant Branch (AGB) phase leads to a CSPN initial mass estimate of $M_{\text{ini}} = 5.12^{+0.16}_{-0.15}$. The initial mass errors reflect the errors in the cluster physical parameters. This is one of the highest CSPM progenitor masses determined to date with decent accuracy (e.g., V. Fragkou et al. 2019b).

5.2. The Planetary Nebula PHR J1724-3859

Due to cluster velocity dispersions being typically very low ($\leq 1\text{-}3\text{ km s}^{-1}$) with some exceptions (C. Soubiran et al. 2018; Y. Tarricq et al. 2021), a key property for the physical association of a PN with a cluster is the close agreement of their radial velocities. For this reason, we measured a precise nebular radial velocity using our high-resolution HRS and GHOST data. The resolution of GHOST was empirically estimated from the $\lambda 6300\text{\AA}$

and $\lambda 6364\text{\AA}$ sky lines of the gc_sky and gd_sky sky pointings, which are free from nebular emission. These should normally give a radial velocity equal to zero with deviations from this value due to the instrumental resolution. We derive a mean GHOST resolution and thus, radial velocity precision, of 0.04 km s⁻¹, more than enough for our purposes.

For each one of our nebular pointings, we applied Gaussian fits to the stronger nebular emission lines (the [N II] $\lambda 6548, 6584\text{\AA}$ doublet and the H α line) using the IRAF task SPLIT. After determining their peak wavelengths and thus, their Doppler-shifts we determined the nebular radial velocity for each pointing.

The [N II] $\lambda 6548, 6584\text{\AA}$ and H α lines of pointing gd are split, while the same applies for just the [N II] $\lambda 6548, 6584\text{\AA}$ lines of pointings hb, hc, gc and gf (see Figure 4). This simply reflects the internal nebular expansion velocity. Lines that are split into two components, often evident in high-resolution PNe spectra, allow not just an estimate of the PNe expansion velocity, but a more precise determination of radial velocity. This is because their peak is not biased towards the brightest component of front and back expansion (R. Vázquez 2012). The radial velocity for each pointing was estimated as the mean of the radial velocities calcu-

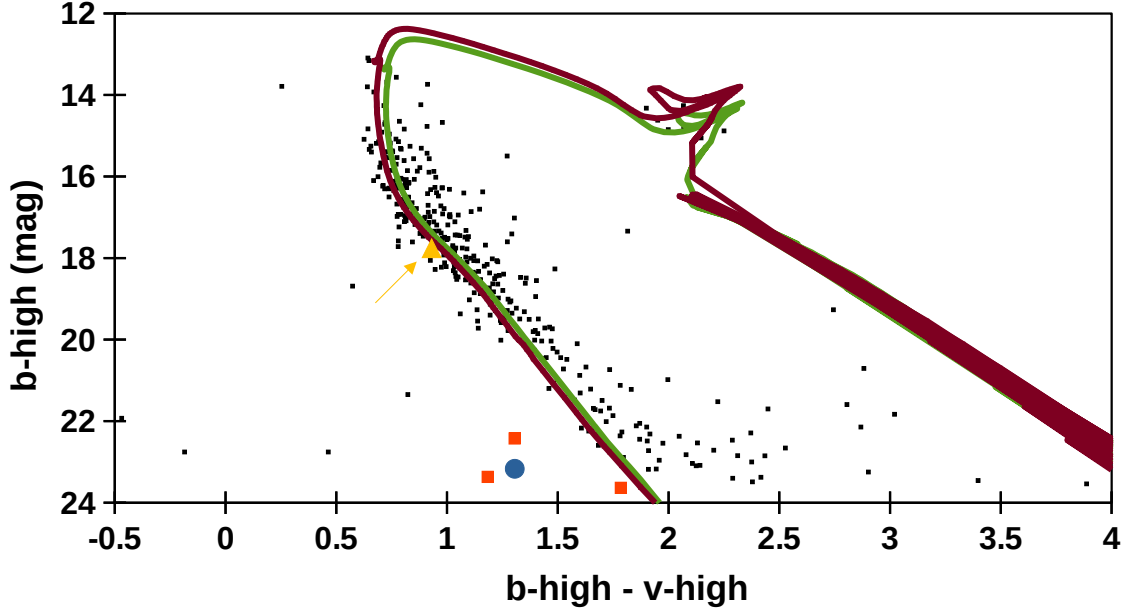


Figure 3. The Trumpler 25 CMD constructed from FORS2 photometric b-high and v-high data of stars with cluster membership probability of 100 % (M. G. J. van Groenigen et al. 2023). The green and brown lines are the theoretical isochrones produced from the cluster literature mean parameters and the ASteCa code, respectively. Although they both present a good fit, the ASteCa code presents a slightly better fit to our data. The data are not extinction corrected, with the interstellar extinction being incorporated in the fitted isochrones. The light red squares and blue circle depict the only blue stars within the nebula field. These were not part of the original cluster CMD that was used for the isochrone fit since they are too faint to be detected with Gaia. Their colour uncertainties (ranging from 0.15 to 0.22) do not affect their identification as evolved stars. The blue circle shows the location on the CMD of the blue star that is closest to the nebula apparent centre that we identify as the true CSPN. The yellow triangle (whose position in the plot is shown by the yellow arrow) indicates the location of the star that has been previously falsely identified as the CSPN by I. González-Santamaría et al. (2021). It is evident that this star is not lying bluewards the MS (even if considering its colour uncertainty of 0.02) and towards fainter magnitudes as it would be expected for an evolved star as a CSPN.

lated from each $[\text{N II}]\lambda 6548, 6584\text{\AA}$ and $\text{H}\alpha$ line present, while its assigned uncertainty implies the spread of the radial velocities calculated from the different emission lines. In the case of pointings gb and ge sky subtraction is problematic due to the sky exposures being acquired more than a month later and thus, for these pointings we excluded the $\text{H}\alpha$ line in the calculation of their radial velocities. In the case of split lines, we initially measured the peak of each component separately and then calculated their average. The $\text{H}\alpha$ line is not detected in pointing gc due to the relatively low surface brightness of the PN at this pointing. Table 2 shows our radial velocity estimates for each pointing. The radial velocity spread in different pointings reflects the internal movement of the nebular gas.

The systemic nebular radial velocity, estimated as the mean from all nebular pointings is $-20.0 \pm 0.7 \text{ km s}^{-1}$ with a standard deviation of 1.9 km s^{-1} . Taking into consideration only the emission lines that present a split, which have more precise peaks (see above), we estimate a systemic nebular radial velocity of $-19.4 \pm 0.7 \text{ km s}^{-1}$

very close to the previous value. Taking into account only the HRS and GHOST data separately, we estimate a PN radial velocity of $-19.9 \pm 1.0 \text{ km s}^{-1}$ and $-20.1 \pm 1.0 \text{ km s}^{-1}$ respectively, confirming the accuracy of our method and so the robustness of the PN radial velocity estimate.

We also measured the nebular expansion velocity for each HRS and GHOST pointing (see Table 1) from the split of the $[\text{N II}]$ lines and the full width half maximum (FWHM) of the $\text{H}\alpha$ line, taking into consideration the thermal broadening estimated using the $\lambda 6300\text{\AA}$ night-sky line. To specify, the expansion velocity for pointings hb, hc, gc and gd (which present a split and have problematic or no $\text{H}\alpha$ detection) was measured from their $[\text{N II}]$ line splitting and for pointings ha, hd, ga, gb, ge (that do not present a split) from the FWHM of their $\text{H}\alpha$ line, while for pointing gf (which presents both a prominent split of the $[\text{N II}]$ lines and a solid $\text{H}\alpha$ detection) as the average calculated with both methods. HRS and GHOST can attain a similar velocity precision and thus, using the data from all HRS and GHOST

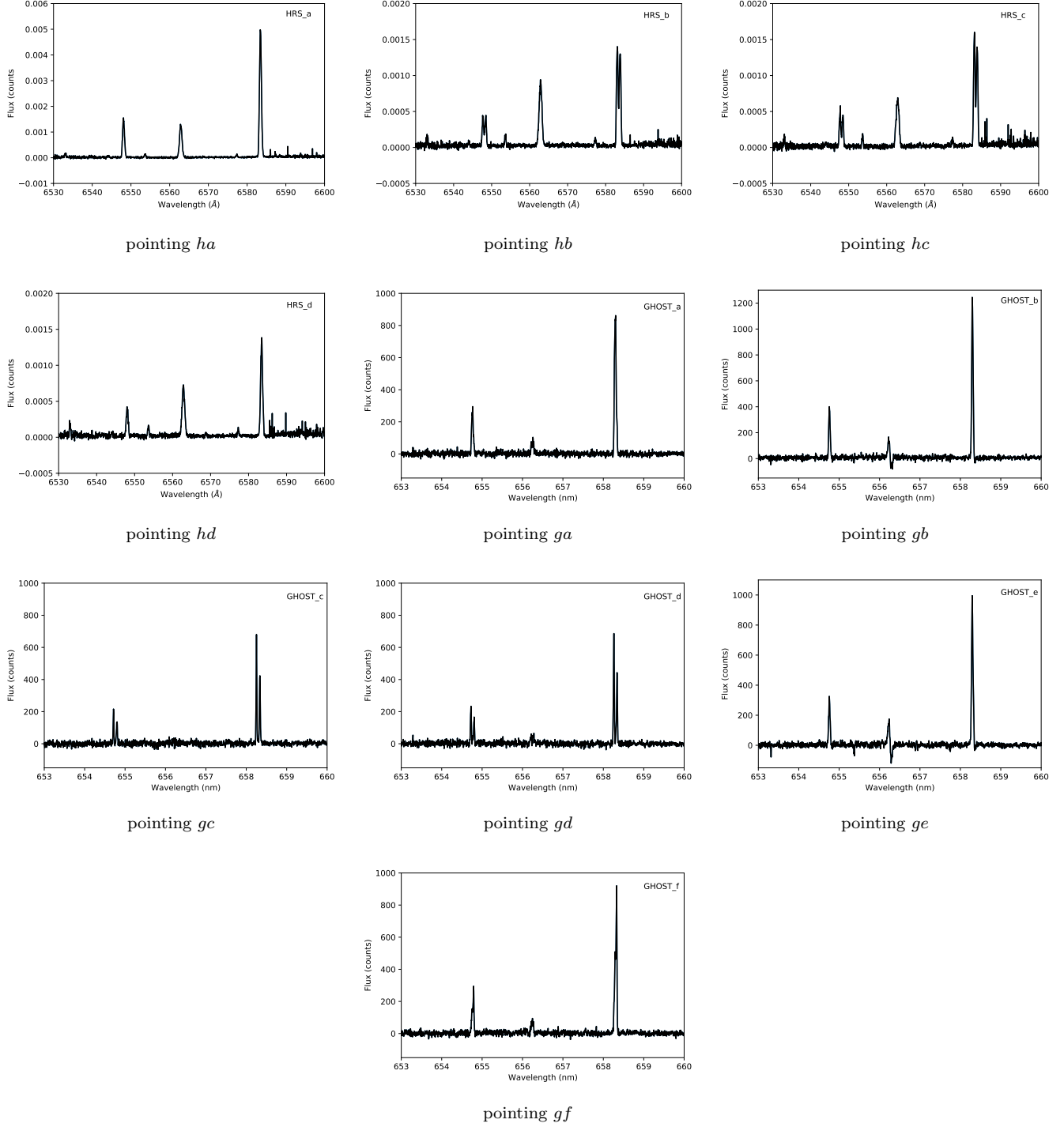


Figure 4. The HRS and GHOST reduced 1-D spectral data showing the $[\text{N II}]\lambda 6548, 6584\text{\AA}$ doublet and $\text{H}\alpha$ line for HRS pointings ha-hd and GHOST pointings ga-gf. The $[\text{N II}]\lambda 6548, 6584\text{\AA}$ lines present a prominent split in the spectra of pointings hb, hc, gc, gd and gf, while the same is true for the $\text{H}\alpha$ line in the spectrum of pointing gd.

pointings, we calculate a mean nebular expansion velocity of 21 km s^{-1} with $\sigma = 5 \text{ km s}^{-1}$. Applying the correction factor from R. Jacob et al. (2013) to account for the fact that the velocity of the nebular outer edges cannot be determined from spectral data, we estimate a

corrected nebular expansion velocity of 31 km s^{-1} with $\sigma = 8 \text{ km s}^{-1}$, completely typical for a PN.

Due to the problematic sky subtraction (see Section 4) of our FORS2 spectra (see Figure 5), we cannot use the FORS2 data for estimating the PN reddening. HRS

Table 2. The derived PN radial and expansion velocities, $[\text{N II}]/\text{H}\alpha$ and $[\text{S II}] I(6731)/I(6716)$ ratios, and N_e for each pointing

ID	$v_r \pm \sigma$ (km s ⁻¹)	v_{exp} (km s ⁻¹)	$[\text{NII}]/\text{H}\alpha^{\text{a}}$	$I(6731)/I(6716)^{\text{b}}$	N_e^{c} (cm ⁻³)
ha	-19.6±1.9	28			
hb	-20.1±2.2	17			
hc	-19.6±1.9	17			
hd	-20.3±1.6	28			
ga	-19.0±4.7	29	11.6	0.71±0.09	<100
gb	-21.1±1.3	16		0.61±0.07	<100
gc	-22.8±1.4	19		0.98±0.11	657±330
gd	-19.5±1.3	17	9.6	0.53±0.13	<100
ge	-22.3±1.5	18		0.65±0.08	<100
gf	-15.8±1.7	19	9.3	0.87±0.12	378±270
fors2			12.6 ^d	0.75±0.16	<100

^aUncorrected for extinction. Corresponding ratios not estimated for: a) pointings gb and ge due to the problematic sky subtraction of their frames, b) pointing gc due to the absence of the $H\alpha$ line, c) all HRS pointings since HRS spectra is neither sky subtracted nor flux calibrated.

^bHRS pointings have no assigned $I(6731)/I(6716)$ ratios and N_e due to the corresponding data being neither sky subtracted nor flux calibrated, rendering the calculation of these parameters not optimal.

^cAssuming $T_e = 10000$ K

^dOver-subtraction of the $H\alpha$ line due to sky contamination. The true $[\text{NII}]/\text{H}\alpha$ ratio is likely lower than this.

and GHOST spectra are not flux calibrated, so are also inadequate for calculating the nebular reddening. Our spectral data, used for the following calculations, are not corrected for interstellar extinction due to the lack of a reliable PN reddening measured directly from them. Since the spectral lines used for the calculation of the corresponding line ratios are sufficiently close, this is not expected to significantly affect our results.

For estimating the nebular electron density N_e , Gaussian fits were also applied to the $[\text{S II}] \lambda 6716, 6731 \text{ \AA}$ doublet that was detected in our GHOST (see Figure 6) and FORS2 spectra, in order to measure the corresponding $[\text{S II}] \lambda 6731/6716 \text{ \AA}$ ratios. HRS will not be used for N_e because it is neither flux-calibrated nor sky-subtracted. While GHOST data are not flux calibrated and FORS2 data suffer from modest sky subtraction issues, these issues alone are not expected to substantially affect the estimation of the $[\text{S II}] \lambda 6731/6716 \text{ \AA}$ ratio, since the $[\text{S II}]$ lines are very close to each other and their ratio is not significantly affected by sky emission at different velocity. In the spectrum of pointing gd, both $[\text{S II}] \lambda 6716 \text{ \AA}$ and $\lambda 6731 \text{ \AA}$ lines present a split as for other lines and so the emission of each component was measured separately and then added to estimate their total emission. The nebular electron density was estimated for each GHOST pointing and FORS2 data from their $[\text{S II}] \lambda 6731/6716 \text{ \AA}$ ratio and the TEMDEN task in PYNEB (V. Luridiana et al. 2015), assuming a $T_e = 10000$ K (see Table 2). The lines used for the derivation of the electron density are not corrected for extinction. This does not limit the analysis as their wave-

lengths are sufficiently close that extinction should not effect the observed ratio. The $[\text{S II}] \lambda 6731/6716 \text{ \AA}$ doublet is not sensitive enough to derive a precise electron density close to the low density limit (D. E. Osterbrock & G. J. Ferland 2006). For most of our pointings the PN nebular density was found to be at the low density limit of $N_e < 100 \text{ cm}^{-3}$. Two of our pointings (gc and gf) do have a larger electron density due to local density variations. The nebular mean electron density was estimated using the mean $[\text{S II}] \lambda 6731/6716 \text{ \AA}$ ratio, calculated from all GHOST pointings plus FORS2. The mean $[\text{S II}] \lambda 6731/6716 \text{ \AA}$ ratio was found to be equal to 0.73 ± 0.04 and thus, the mean electron density is also estimated to be $N_e < 100 \text{ cm}^{-3}$ and close to the low density limit.

The $[\text{N II}]/\text{H}\alpha$ line ratio was also estimated from the spectral data of some of the GHOST pointings, and the FORS2 data (see Table 2). HRS pointings were not employed for this purpose due to their limitations in the calculation of line ratios (see above). Pointings gb and ge suffer from over-subtraction of the geocoronal $H\alpha$ emission line due to problematic sky subtraction in the case of these two science pointings, and there is no $H\alpha$ detection in the spectrum of pointing gc, so the $[\text{N II}]/\text{H}\alpha$ line ratio was also not derived for these. From the ga, gd and gf GHOST pointings we estimate a mean $[\text{N II}]/\text{H}\alpha = 10.2$, while from our FORS2 data we estimate a $[\text{N II}]/\text{H}\alpha = 12.6$. In the case of the FORS2 data, the quoted $[\text{N II}]/\text{H}\alpha$ ratio is likely higher than the true value as a result of the over-subtraction of the $H\alpha$ line in our data due to the sky contamination present

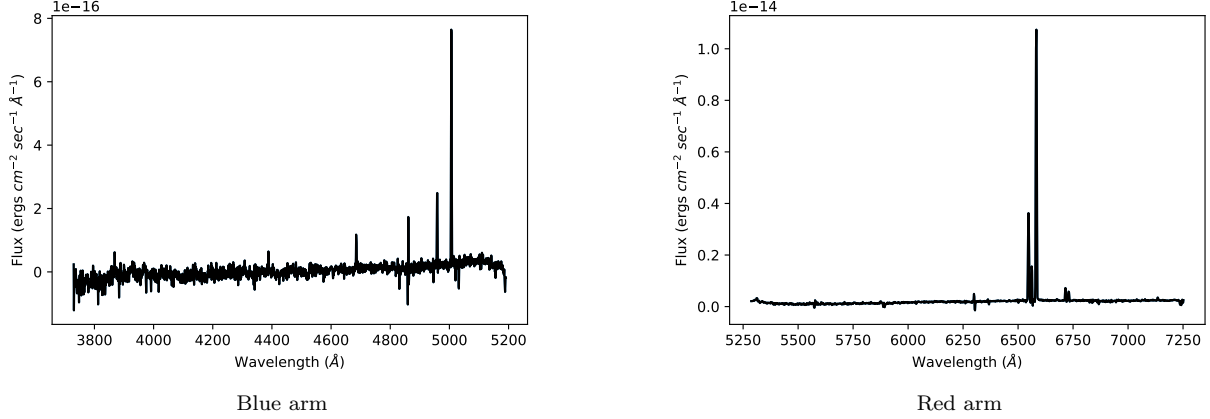


Figure 5. The FORS2 blue arm (left panel) and red arm (right panel) 1-D spectra. Modest sky line over-subtraction is evident, especially in the blue arm. The high excitation He II $\lambda 4686\text{\AA}$ emission line and $H\beta$, [O III] $\lambda 4959, 5007\text{\AA}$, [N II] $\lambda 6548, 6563\text{\AA}$, $H\alpha$ and [S II] $\lambda 6716, 6731\text{\AA}$ lines are clearly identified.

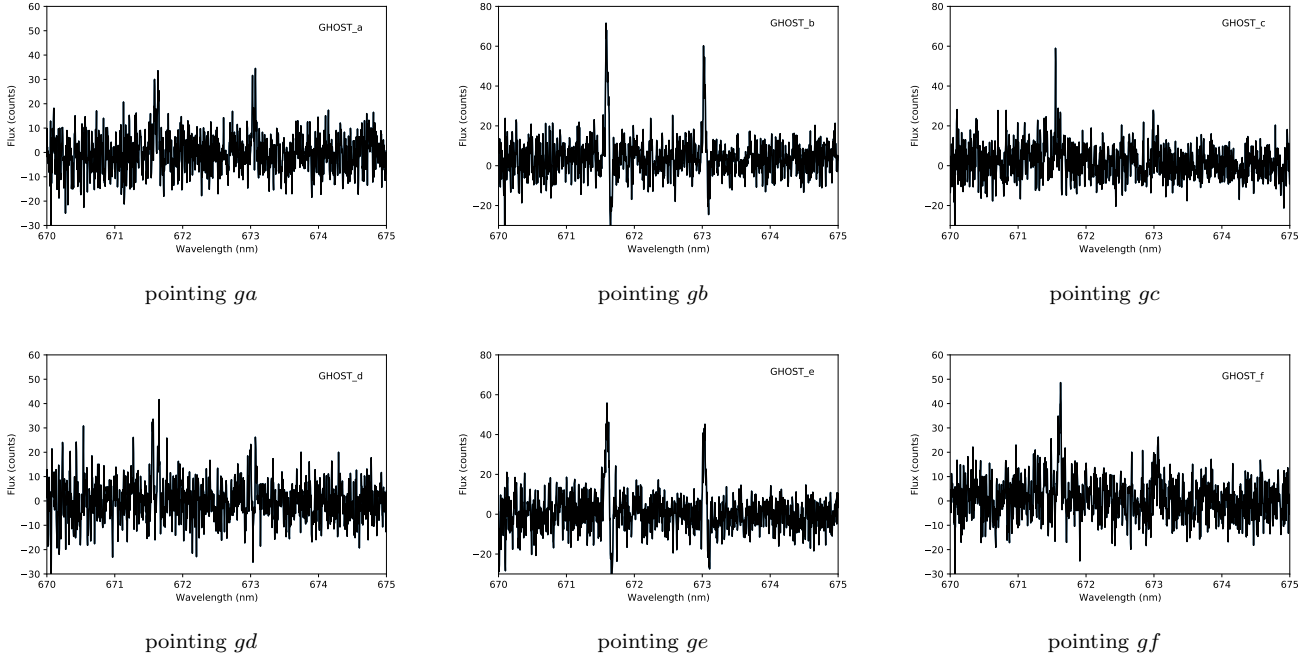


Figure 6. The 1-D spectra of all GHOST pointings, depicting the [S II] doublet. A small over-subtraction issue is evident in the spectra of pointings gb and ge.

in the FORS2 science frames. From our FORS2 data we, also, estimate a [O III]/ $H\beta$ line ratio of 8, which also should be considered as an upper limit and note the presence of the high excitation He II $\lambda 4686\text{\AA}$ emission line (see Figure 5). For a further discussion about the nebular estimated emission line ratios, see Section 6.

5.3. The Central Star of PHR J1724-3859

I. González-Santamaría et al. (2021) and N. Chornay & N. A. Walton (2021) have reported the identification

of many putative CSPN using Gaia data, including that for PHR J1724-3859. The yellow triangle (marked by the yellow arrow) in Figure 3 indicates the location of the CSPN identified by I. González-Santamaría et al. (2021) on our FORS2 CMD. It is noted that in our CMD (see Figure 3) the identified star does not lie where it should if being the true CSPN (i.e. in the fainter part of the diagram and bluewards from the MS, as expected for evolved stars). Although this star is the bluest Gaia detected star in the field, and indeed the major basis

on which CSPN were chosen (I. González-Santamaría et al. 2021), the true CSPN is fainter. Indeed, (Q. A. Parker et al. 2022) have shown that many true CSPNe are beyond GAIA limits ($g \sim 21$). The approach adopted by both I. González-Santamaría et al. (2021) and N. Chornay & N. A. Walton (2021) leads to an estimated 20% CSPN misidentification rate (Q. A. Parker et al. 2022). For these reasons, we make an effort to identify afresh the true CSPN of PHR J1724-3859 using our much deeper FORS2 data.

By over-plotting all FORS2 photometrically identified stars in the nebula field on our cluster CMD, we note stars that lie bluer than the MS where their colours and magnitudes are consistent with these of white dwarfs (as indicated with a blue circle and light red squares in Figure 3). We found only four blue stars in the nebular field (see Figure 7). The one that lies closest to the projected apparent PN geometric centre (indicated with a blue circle in Figure 3 and Figure 7), is deemed the true CSPN with J2000 position RA: 17h24m29.904s, DEC: $-38^{\circ}59'47.15''$. This is only ~ 2.6 arcseconds to the West from our estimated geometric centre for a PN that is 156×96 arcseconds in angular extent. The previously identified CSPN is offset ~ 7 arcseconds from the PN centroid to the North West. The blue stars identified here are not originally part of the cluster CMD because they are beyond the reach of Gaia. The brightest putative CSPN identified by I. González-Santamaría et al. (2021) is within 2 arcsec of our newly identified CSPN (see Figure 8).

SExtractor can perform photometric measurements for many sources automatically and thus, is an efficient method for constructing cluster CMDs and to explore the deviation of stellar colours from the MS. However, the calculated magnitudes may not be precise for very dim stars in a crowded field, as is the case of the newly identified CSPN. Therefore, the b-high and v-high magnitudes of our CSPN, were measured again manually with aperture photometry and the IRAF task DAOPHOT/QPHOT. This is after applying aperture correction and carefully selecting the appropriate aperture radius (1 arcsec), annulus (1 arcsec) and dannulus (0.5 arcsec) for the specific star and using the appropriate zeropoints for each filter. Using the same parameters and method, we also estimated the u-high, Bessel R special and Bessel I magnitudes. The estimated b-high, v-high, Bessel R special and Bessel I magnitudes were then corrected for atmospheric extinction, while a colour term correction was also applied (see Section 4). The measured u-high magnitude was calibrated by cross-correlation with the A. Pickles & É. Depagne (2010) U magnitudes, as before (see Section 4). We find u-high

$= 24.5 \pm 0.4$ mag, b-high $= 24.5 \pm 0.3$ mag, v-high $= 23.9 \pm 0.1$ mag, Bessel R special $= 23.5 \pm 0.4$ mag and Bessel I $= 22.8 \pm 0.2$ mag. The more precise manually measured b-high and v-high CSPN magnitudes are somewhat fainter than those measured with SExtractor due to the special care taken to avoid contamination from nearby stellar emission.

Theoretically, a CSPN effective temperature for a PN that has He II $\lambda 4686\text{\AA}$ high-excitation line emission, like PHR J1724- 3859, is expected to be between ~ 50 to up to 300 kK (see, M. M. Miller Bertolami 2016; G. H. Jacoby et al. 2017) though no known PN has a temperature beyond 250 kK. Under this consideration and using the Astrolib PySynphot package⁵ (STScI Development Team 2013), we derive the expected B-V colour for stars with effective temperatures from 50 to 300 kK. To specify, within the PySynphot/Observation module we generated a blackbody spectrum using the BlackBody class, for temperatures 50 to 300 kK (in steps of 5 kK), assuming zero extinction. The B and V synthetic magnitudes in the VEGA system have consequently been obtained for each temperature using the ObsBandpass function. The B-V colour has finally been estimated by subtracting the calculated synthetic B and V magnitudes for each temperature and taking their mean, assigning as error the semi-range of the computed B-V values. Using the mean modelled colour and the b-high - v-high colour of our CSPN, we estimate a CSPN reddening and thus, a PN reddening of $E(B-V) = 0.92 \pm 0.33$ (assuming the PN reddening is identical to the CSPN reddening). We use this PN reddening value in the following analysis, when relevant. Correcting all our CSPN magnitudes for interstellar extinction, using the J. A. Cardelli et al. (1989) extinction curve with $R_v = 3.1$ (J. E. O'Donnell 1994), we find u-high $= 20.1 \pm 1.1$ mag, b-high $= 20.7 \pm 1.1$ mag, v-high $= 21.1 \pm 1.0$ mag, Bessel R special $= 21.2 \pm 1.1$ mag and Bessel I $= 21.1 \pm 1.1$ mag.

6. ANALYSIS & DISCUSSION

The PN systemic radial velocity of -20.0 km s^{-1} with $\sigma = 1.9 \text{ km s}^{-1}$, estimated in Subsection 5.2, is close, within the errors, to the cluster's mean radial velocity of -25.5 km s^{-1} given the unusually large OC velocity dispersion for Trumpler 25 that these robust Gaia data provide of $\sigma = 9.1 \text{ km s}^{-1}$. This provides strong evidence in support of PN cluster membership. The PN reddening, as estimated from the CSPN colour (see Subsection 5.3), also matches, within the errors providing further

⁵ Lim, P. L., Diaz, R. I., & Laidler, V. 2015, PySynphot User's Guide (Baltimore, MD: STScI), <https://pysynphot.readthedocs.io/en/latest/>

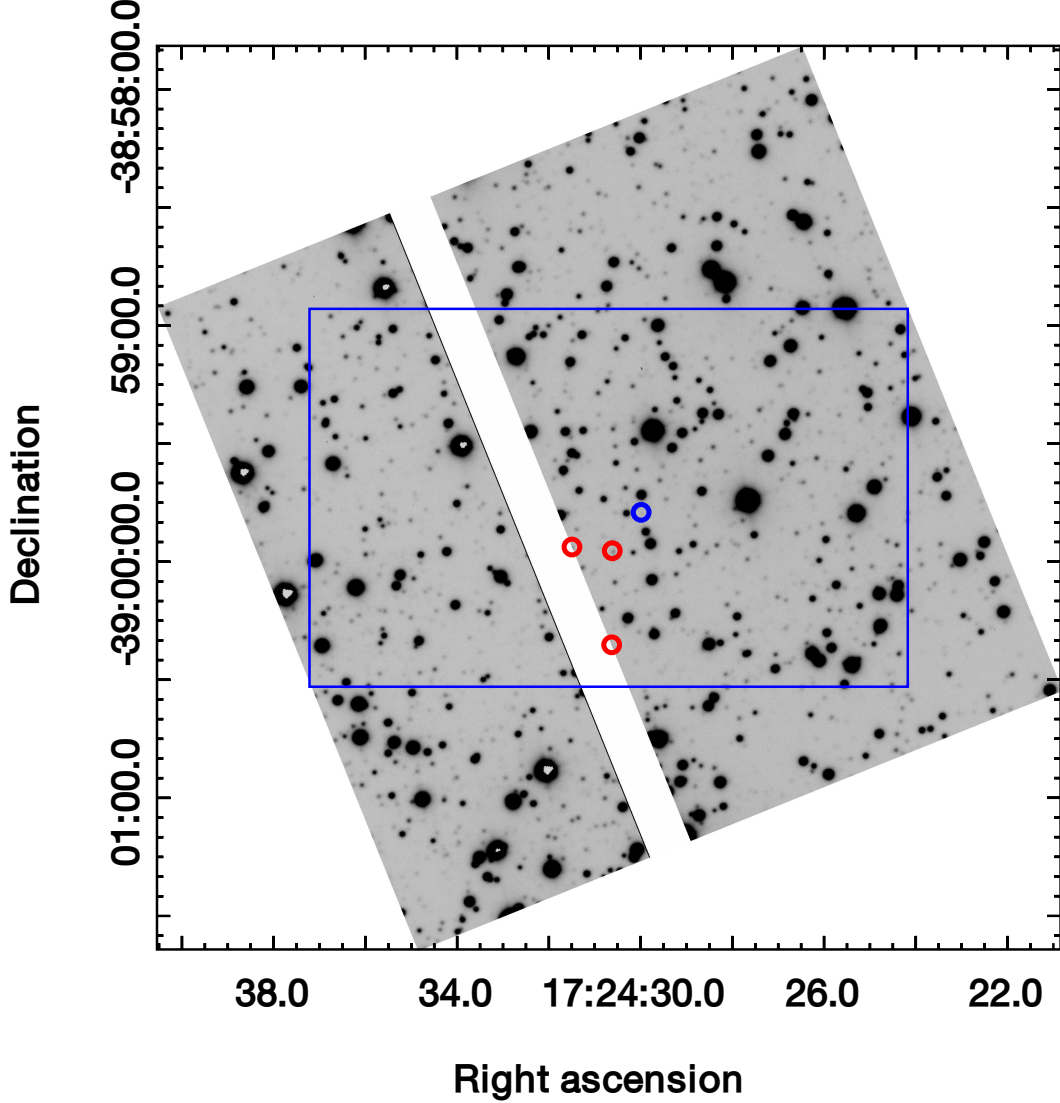


Figure 7. A v-high $30 \times 30 \text{ arcsec}^2$ FORS2 image centred on the PN’s apparent centre. The blue rectangle indicates the position and size of the PN. The blue and red circles show all blue stars in the nebular field. The blue circle indicates the blue star we have newly identified as the CSPN that lies closest to the nebular apparent centre.

support for the physical association of the two objects. Taking the mean PN angular radius of 62 arcsec and its integrated $H\alpha$ flux of $\log F(H\alpha) = -12.17 \text{ mW/m}^2$ (see Section 1) corrected for extinction (from adopting the PN reddening as determined from the CSPN colour), we find an extinction corrected $\log F(H\alpha)$ of -11.20 . We use this to estimate a PN statistical distance, using the Surface-Brightness radius (SB-r) relation of (D. J. Frew et al. 2016), of $2194 \pm 500 \text{ pc}$, which also agrees well with the accurate Gaia based cluster distance of $2417 \pm 14 \text{ pc}$ given the typical $\sim 20\%$ error of the SB-r technique.

Adopting the Gaia cluster mean distance of 2417 pc and the PN mean apparent diameter of 124 arcsec , we

estimate a PN physical size of $1.78 \times 1.12 \text{ pc}$ and a PN mean physical radius of $0.726 \pm 0.004 \text{ pc}$. Considering the derived nebular expansion velocity of 31 km s^{-1} , estimated in Subsection 5.2, we obtain a PN kinematic age of $23000 \pm 6000 \text{ years}$, confirming the highly evolved nature of the PN. The PN kinematic age and so physical size and volume, justifies the PN nebular density that for most of our pointings was found to be at the low density limit of $N_e < 100 \text{ cm}^{-3}$. From the $H\alpha/H\beta$ standard ratio of 2.85, we find an extinction corrected nebular $H\beta$ flux of $\log F(H\beta) = -11.66 \text{ mW/m}^2$. Following R. L. M. Corradi et al. (2015) and using the absolute nebular $H\beta$ flux of -11.66 mW/m^2 , the electron density

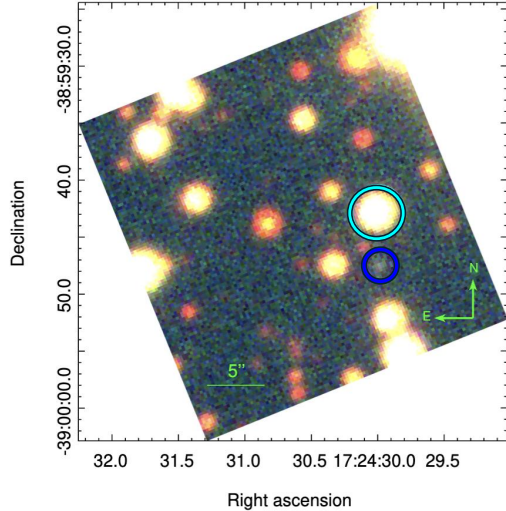


Figure 8. A $30 \times 30 \text{ arcsec}^2$ FORS2 RGB (R is v-high, G is b-high and B is u-high) image showing the identified CSPN with J2000 position RA: 17h24m29.904s, DEC: -38°59′47.15″. The dark blue circle shows the location of the true CSPN newly identified here, while the light blue circle shows the one identified by [I. González-Santamaría et al. \(2021\)](#). The two stars are within 2 arcsec of each other.

of $N_e < 100 \text{ cm}^{-3}$ as determined in Subsection 5.2, the adopted cluster distance of 2417 pc and the effective recombination coefficient of $H\beta$ from [D. E. Osterbrock & G. J. Ferland \(2006\)](#), we estimate a nebular ionized mass larger than $0.11 M_\odot$.

The average $[\text{N II}]/\text{H}\alpha$ line ratio, as estimated from the GHOST spectral data, is 10.2, much higher than typical for PNe (see, [R. L. Kingsburgh & M. J. Barlow 1994](#)) and indicative of Type-I chemistry ([M. Peimbert & S. Torres-Peimbert 1983](#)). This is also supported by the detection of the He II $\lambda 4686\text{\AA}$ high excitation emission line, the very high CSPN effective temperature (see below), and the bipolar nebular shape.

Using our derived CSPN V magnitude, PN reddening (see Subsection 5.3) and the adopted cluster distance, we estimate a CSPN absolute magnitude of $M_v = 9.15 \pm 1.03$. The CSPN final mass was derived by over-plotting its absolute magnitude and PN kinematic age along with the [M. M. Miller Bertolami \(2016\)](#) evolutionary tracks for $Z=0.02$. We estimate a final mass of $M_{fin} = 0.95 \pm 0.12 M_\odot$, with the assigned error reflecting the absolute magnitude and kinematic age errors.

To estimate the CSPN effective temperature, we over-plot the corresponding luminosities for the estimated CSPN absolute magnitude and CSPN effective temperatures from 50 to 300 kK (i.e. the range of possible CSPN temperatures as predicted from theory, see Subsection 5.3) in steps of 10 kK, along with the corre-

sponding [M. M. Miller Bertolami \(2016\)](#) evolutionary tracks (see, [V. Fragkou et al. 2022](#)). We derive a CSPN effective temperature of $250 \pm 50 \text{ kK}$, which is much higher than average and also indicative of Type I PN chemistry and an intermediate progenitor mass (see, [V. Fragkou et al. 2019b](#)). The assigned temperature error reflects the uncertainties associated with the CSPN absolute magnitude. The CSPN effective temperature was also estimated following the Zanstra method ([H. Zanstra 1931](#)) and using the absolute nebular $H\beta$ flux, the He II $\lambda 4686\text{\AA}/H\beta$ ratio of 1.13 (estimated as an upper limit from our FORS2 data) and the CSPN V magnitude, all corrected for extinction, finding a Zanstra $T_{\text{eff}}(\text{HI}) = 253 \pm 76 \text{ kK}$ (adopting a 30% error) and a Zanstra $T_{\text{eff}}(\text{He II}) < 290 \text{ kK}$, in excellent agreement with the CSPN effective temperature calculated previously from the evolutionary tracks. The estimated CSPN luminosity for an effective temperature of $253 \pm 76 \text{ kK}$, is $\log L/L_\odot = 1.96 \pm 0.55$. The estimated physical parameters of both the cluster Trumpler 25 and the PN PHR J1724-3859 are presented in Table 3.

The initial-to-final mass relation (IFMR) is traditionally constructed from cluster white dwarfs (e.g., [J. D. Cummings et al. 2018](#)) and links their physical properties to those of their progenitor stars, determined independently from cluster studies. Cluster PNe can offer additional key data points to contribute in the establishment of a distinct IFMR that is currently poorly constrained, which is crucial in tracing the enrichment of essential elements, such as carbon and nitrogen, in our Galaxy and beyond. Figure 9 shows our new cluster PN point (i.e. the initial and final masses of the CSPN of PHR J1724-3859 estimated above) and all other points derived from our other PNe associated with open clusters ([V. Fragkou et al. 2019a,b, 2022](#)) over-plotted along with the latest IFMR estimates from cluster WDs and semi-empirical “PARSEC” fit ([J. D. Cummings et al. 2018](#)) and the [T. Cunningham et al. \(2024\)](#) IFMR derived from a volume-limited 40 pc sample of WDs using population synthesis modelling. Our new data point, depicted in orange, falls in the sparsely populated intermediate initial mass area of the IFMR, and agrees, within the errors, with both the predictions from cluster white dwarfs and population synthesis models, and the other open cluster PN points (see Table 4). All open cluster-PN points fall slightly lower, by $\sim 0.1 M_\odot$, than the general trend from [J. D. Cummings et al. \(2018\)](#), a systematic effect that deserves to be further explored in future studies and possibly associated with the evolutionary tracks employed for the estimation of final masses. The [T. Cunningham et al. \(2024\)](#) IFMR seems to better fit our data for intermediate initial masses (with our new

Table 3. Estimated physical properties of the PN PHR J1724–3859 and the open cluster Trumpler 25.

Parameter	PN PHR J1724–3859	Trumpler 25
RA (J2000) (1)	17:24:30.70	17:24:30.70
DEC (J2000) (1)	–38:59:43.91	–39:01:25.00
Apparent size (arcsec ²) (2),(3)	152×96	576 (diam.)
Physical size (pc) (4)	1.78×1.12	
Physical radius (pc) (4)	0.726 ± 0.004	3.37
Radial velocity (km s ^{–1}) (5),(6)	–20.0, $\sigma = 1.9$	–25.5, $\sigma = 9.1$
Distance (kpc) (7),(8)	2.2 ± 0.5	2.4 ± 0.01
Reddening $E(B - V)$ (9),(10)	0.92 ± 0.33	0.85 ± 0.01
Expansion velocity (km s ^{–1}) (11)	31, $\sigma = 8$	
Chemistry (12)	Type I	[Fe/H] = 0.17 ± 0.02
Ionised mass (M_{\odot}) (15)	>0.11	
Electron density N_e (cm ^{–3}) (16)	<100	
log(H α) flux (mW/m^2) (17)	–12.17 ± 0.12	
T_{eff} (kK) (18)	250 ± 50	
Zanstra T(H I) (kK) (19)	253 ± 76	
Zanstra T(He II) (kK) (20)	<290	
Luminosity log L/L_{\odot} (21)	1.96 ± 0.55	
Initial mass (M_{\odot})	5.12 ^{+0.16} _{–0.15}	
Final mass (M_{\odot})	0.95 ± 0.12	
pmRA (mas yr ^{–1}) (22)		0.315 ± 0.002
pmDec (mas yr ^{–1}) (22)		–2.138 ± 0.002
CSPN magnitudes (U,B,V,R,I) (23)	20.1–21.2	
Absolute magnitude M_V (24)	9.15 ± 1.03	
Age (13),(14)	23 ± 6 kyr	112 ± 9 Myr

NOTE— (1) HASH database (Q. A. Parker et al. 2016). (2) PN apparent size from Q. A. Parker et al. (2006). (3) Cluster diameter from N. V. Kharchenko et al. (2013). (4) Computed for the adopted cluster distance. (5) PN radial velocity from GHOST+HRS data. (6) Cluster RV from Gaia DR3 (M. G. J. van Groenningen et al. 2023). (7) PN statistical distance (D. J. Frew et al. 2016). (8) Cluster distance from Gaia parallaxes (M. G. J. van Groenningen et al. 2023). (9) PN reddening from CSPN colour. (10) Cluster reddening from AsteCa isochrone fit. (11) Expansion velocity from GHOST/HRS line splitting and H α FWHM. (12) Cluster metallicity from AsteCa isochrones ($Z = 0.023 \pm 0.001$). (13) PN age from radius, velocity, and distance. (14) Cluster age from Padova isochrones. (15) Nebular mass from R. L. M. Corradi et al. (2015). (16) Electron density from [S II] ratio assuming $T_e = 10^4$ K. (17) H α flux from D. J. Frew et al. (2013). (18) Derived from M. M. Miller Bertolami (2016) tracks. (19) Zanstra temperature (H I). (20) Upper limit from He II $\lambda 4686/H\beta$. (21) Luminosity using Zanstra T(HI). (22) Gaia DR3 proper motions. (23) CSPN magnitudes from FORS2 photometry. (24) Absolute magnitude from cluster distance and PN reddening.

cluster PN point falling above their trend) but unlike an empirical or semi-empirical IFMR, derived from cluster WDs (e.g., J. D. Cummings et al. 2018), it does not implicitly include the effects of stellar rotation and magnetic fields that could affect the final masses of mainly intermediate and higher mass stars.

7. CONCLUSIONS

PNe that are physical members of star clusters are very rare, but due to their importance in stellar evolution studies, any additional detection is highly significant.

Using data acquired from a series of large telescopes we identified the CSPN of the proposed new OC-PN

pair and estimated its physical properties along with the properties of its progenitor, the PN PHR J1724-3859 and the host cluster Trumpler 25.

Using our high-resolution spectra we showed that the PN PHR J1724-3859 has a mean systemic radial velocity of -20.0 km s^{–1} with $\sigma=1.9$ km s^{–1} very close to that of the open cluster Trumpler 25 which has been estimated to be -25.5 km s^{–1} with $\sigma=9.1$ km s^{–1} from Gaia DR3 data. This is key evidence supporting the physical association of the two objects given the cluster has an unusually large, but robustly determined, velocity dispersion. Then taking into account the good agreement of the estimated OC-PN reddening and the independently estimated PN and cluster distances, the

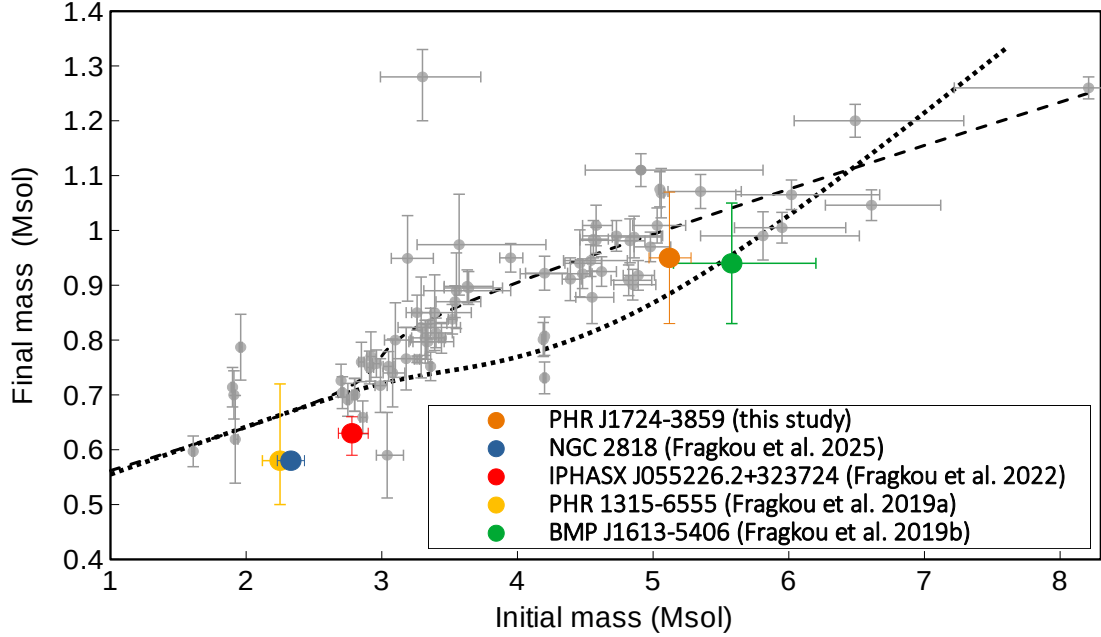


Figure 9. Our open cluster PN points (coloured filled circles) over-plotted along the IFMR "PARSEC" trend (dashed line) of the [J. D. Cummings et al. \(2018\)](#) data points (grey filled circles). The latest IFMR estimated by [T. Cunningham et al. \(2024\)](#) using population synthesis modeling is shown by the dotted line.

Table 4. The initial and final masses of all open cluster PNe.

PN	CSPN M_{ini} (M_{\odot})	CSPN M_{fin} (M_{\odot})
PHR J1724-3859	$5.12^{+0.16}_{-0.15}$	0.95 ± 0.12
PHR 1315-6555 ^a	2.25 ± 0.13	$0.58^{+0.14}_{-0.08}$
BMP J1613-5406 ^b	$5.58^{+0.62}_{-0.43}$	0.94 ± 0.11
IPHASX J055226.2+323724 ^c	$2.78^{+0.12}_{-0.10}$	$0.63^{+0.03}_{-0.04}$
NGC 2818 ^d	2.33 ± 0.10	0.58 ± 0.01

^aFrom [V. Fragkou et al. \(2019a\)](#).

^bFrom [V. Fragkou et al. \(2019b\)](#).

^cFrom [V. Fragkou et al. \(2022\)](#).

^dFrom [V. Fragkou et al. \(2025\)](#).

proximity of the PNe to the cluster core (well within the tidal radius), and plausible derived PN physical parameters, PN cluster membership appears to be highly likely. When the properties of the PN in this new OC-PN pair are also further compared to the four other members of the class, there are striking common properties. All are bipolars, all have Type I chemistry shown by nitrogen enrichments with large $H\alpha$ to $[NII]$ ratios, all are kinematically at extreme limits and all have very hot CSPN. These combined properties are themselves rare amongst the general PNe population (see Table 3 in [V. Fragkou et al. \(2025\)](#)). They are also evolved and have higher than typical progenitor masses. This is explained by the fact that, given the cluster ages, only high mass progenitors can currently form PNe in such clusters. PNe

with low-mass cluster star progenitors are still billions of years away from forming PNe.

Therefore, we conclude that the PHR J1724-3859-Trumpler 25 pair is highly likely to be a real association and include it in our small sample of very rare open cluster-PNe associations.

Our findings again are in mild disagreement with the latest IFMR estimates from cluster WDs from [J. D. Cummings et al. \(2018\)](#) but fit the emerging trend for all our other open cluster-PNe. They also better agree with the [T. Cunningham et al. \(2024\)](#) IFMR from population synthesis models. We are undertaking studies to explore the origin of the systematic effect observed in the final masses of open cluster-PNe, which fall slightly below by $\sim 0.1M_{\odot}$ but effectively parallel to the general trend of cluster white dwarfs ([Parker et al.](#), in prepara-

tion). This could have implications for stellar evolutionary timescales.

ACKNOWLEDGMENTS

VF thanks Fundação Coordenação de Aperfeiçoamento de Pessoal de Nível Superior (CAPES) for granting the postdoctoral research fellowship Programa de Desenvolvimento da Pós-Graduação (PDPG)-Pós Doutorado Estratégico, Edital nº16/2022, Coordenação de Aperfeiçoamento de Pessoal de Nível Superior - Brasil (CAPES) – Finance Code 001 (88887.838401/2023-00) and Fundação de Amparo à Pesquisa do Estado do Rio de Janeiro (FAPERJ) for granting the postdoctoral research fellowships E-26/200.181/2025 and 200.181/2025(304980). QAP thanks the Hong Kong Research Grants Council for GRF research grants 17326116, 17300417 and 17304520. DRG acknowledges FAPERJ (E-26/211.527/2023) and CNPq (315307/2023-4) for partial support.

We made use of NASA’s Astrophysics Data System; the SIMBAD database operated at CDS, Strasbourg, France; Astropy, a community-developed core Python package for Astronomy (T. A. Collaboration et al. 2022); HASH, an online database at the Laboratory for Space Research at HKU federates available multi-wavelength imaging, spectroscopic, and other data for all known Galactic PNe and is available at: <http://www.hashpn.space>.

Some of the observations reported in this paper were obtained with the Southern African Large Telescope (SALT) under program 2019-1-DDT-002 (PI: Q. A. Parker). Others were based on observations collected at the European Southern Observatory under ESO programmes 0103.D-0093(A) and 0103.D-0093(B). More observations were obtained at the international Gemini Observatory, a program (Program ID: GS-2024A-Q-232) of NSF NOIRLab (acquired through the Gemini Observatory Archive), at NSF NOIRLab and processed using

the Gemini IRAF package and DRAGONS (Data Reduction for Astronomy from Gemini Observatory North and South), which is managed by the Association of Universities for Research in Astronomy (AURA) under a cooperative agreement with the U.S. National Science Foundation on behalf of the Gemini Observatory partnership: the U.S. National Science Foundation (United States), National Research Council (Canada), Agencia Nacional de Investigación y Desarrollo (Chile), Ministerio de Ciencia, Tecnología e Innovación (Argentina), Ministério da Ciência, Tecnologia, Inovações e Comunicações (Brazil), and Korea Astronomy and Space Science Institute (Republic of Korea).

This work made use of the University of Hong Kong/Australian Astronomical Observatory/Strasbourg Observatory H-alpha Planetary Nebula (HASH PN) database, hosted by the Laboratory for Space Research at the University of Hong Kong; This research has made use of the SIMBAD database and the VizieR catalogue access tool, CDS, Strasbourg, France (doi: 10.26093/cds/vizieR). The original description of the VizieR service was published in Ochsenbein, Bauer & Marcout (2000).

This work has made use of data from the European Space Agency (ESA) mission Gaia (<https://www.cosmos.esa.int/gaia>), processed by the Gaia Data Processing and Analysis Consortium (DPAC, <https://www.cosmos.esa.int/web/gaia/dpac/consortium>).

Facilities: SALT (HRS), VLT (FOR2), Gemini (GHOST)

Software: HRS pipeline (A. Y. Kniazev et al. 2016, 2017), EsoReflex (W. Freudling et al. 2013), DRAGONS (K. Labrie et al. 2023), Source Extractor (E. Bertin & S. Arnouts 1996) ASteCA (G. I. Perren et al. 2015)

REFERENCES

- Angelo, M. S., Santos, J. F. C., Corradi, W. J. B., & Maia, F. F. S. 2025, MNRAS, 539, 2513, doi: [10.1093/mnras/staf584](https://doi.org/10.1093/mnras/staf584)
- Bertin, E., & Arnouts, S. 1996, A&AS, 117, 393, doi: [10.1051/aas:1996164](https://doi.org/10.1051/aas:1996164)
- Bessell, M. S. 1990, PASP, 102, 1181, doi: [10.1086/132749](https://doi.org/10.1086/132749)
- Bessell, M. S. 2005, ARA&A, 43, 293, doi: [10.1146/annurev.astro.41.082801.100251](https://doi.org/10.1146/annurev.astro.41.082801.100251)
- Bressan, A., Marigo, P., Girardi, L., et al. 2012, MNRAS, 427, 127, doi: [10.1111/j.1365-2966.2012.21948.x](https://doi.org/10.1111/j.1365-2966.2012.21948.x)
- Cantat-Gaudin, T., Jordi, C., Vallenari, A., et al. 2018, A&A, 618, A93, doi: [10.1051/0004-6361/201833476](https://doi.org/10.1051/0004-6361/201833476)
- Cantat-Gaudin, T., Anders, F., Castro-Ginard, A., et al. 2020, A&A, 640, A1, doi: [10.1051/0004-6361/202038192](https://doi.org/10.1051/0004-6361/202038192)
- Cardelli, J. A., Clayton, G. C., & Mathis, J. S. 1989, ApJ, 345, 245, doi: [10.1086/167900](https://doi.org/10.1086/167900)

- Cavallo, L., Spina, L., Carraro, G., et al. 2024, *AJ*, 167, 12, doi: [10.3847/1538-3881/ad07e5](https://doi.org/10.3847/1538-3881/ad07e5)
- Chen, Y., Bressan, A., Girardi, L., et al. 2015, *MNRAS*, 452, 1068, doi: [10.1093/mnras/stv1281](https://doi.org/10.1093/mnras/stv1281)
- Chen, Y., Girardi, L., Bressan, A., et al. 2014, *MNRAS*, 444, 2525, doi: [10.1093/mnras/stu1605](https://doi.org/10.1093/mnras/stu1605)
- Chornay, N., & Walton, N. A. 2021, *A&A*, 656, A110, doi: [10.1051/0004-6361/202142008](https://doi.org/10.1051/0004-6361/202142008)
- Corradi, R. L. M., García-Rojas, J., Jones, D., & Rodríguez-Gil, P. 2015, *ApJ*, 803, 99, doi: [10.1088/0004-637X/803/2/99](https://doi.org/10.1088/0004-637X/803/2/99)
- Crawford, S. M., Still, M., Schellart, P., et al. 2010, in *Society of Photo-Optical Instrumentation Engineers (SPIE) Conference Series*, Vol. 7737, *Observatory Operations: Strategies, Processes, and Systems III*, ed. D. R. Silva, A. B. Peck, & B. T. Soifer, 773725, doi: [10.1117/12.857000](https://doi.org/10.1117/12.857000)
- Crawford, S. M., Crause, L., Depagne, É., et al. 2016, in *Society of Photo-Optical Instrumentation Engineers (SPIE) Conference Series*, Vol. 9908, *Ground-based and Airborne Instrumentation for Astronomy VI*, ed. C. J. Evans, L. Simard, & H. Takami, 99082L, doi: [10.1117/12.2232653](https://doi.org/10.1117/12.2232653)
- Cummings, J. D., Kalirai, J. S., Tremblay, P. E., Ramirez-Ruiz, E., & Choi, J. 2018, *ApJ*, 866, 21, doi: [10.3847/1538-4357/aadfd6](https://doi.org/10.3847/1538-4357/aadfd6)
- Cunningham, T., Tremblay, P.-E., & W. O'Brien, M. 2024, *MNRAS*, 527, 3602, doi: [10.1093/mnras/stad3275](https://doi.org/10.1093/mnras/stad3275)
- Dias, W. S., Monteiro, H., Caetano, T. C., et al. 2014, *A&A*, 564, A79, doi: [10.1051/0004-6361/201323226](https://doi.org/10.1051/0004-6361/201323226)
- Dias, W. S., Monteiro, H., Moitinho, A., et al. 2021, *MNRAS*, 504, 356, doi: [10.1093/mnras/stab770](https://doi.org/10.1093/mnras/stab770)
- Fragkou, V. 2019, PhD thesis, University of Hong Kong
- Fragkou, V., Parker, Q. A., Zijlstra, A., Shaw, R., & Lykou, F. 2019a, *MNRAS*, 484, 3078, doi: [10.1093/mnras/stz108](https://doi.org/10.1093/mnras/stz108)
- Fragkou, V., Parker, Q. A., Zijlstra, A. A., Crause, L., & Barker, H. 2019b, *Nature Astronomy*, 3, 851, doi: [10.1038/s41550-019-0796-x](https://doi.org/10.1038/s41550-019-0796-x)
- Fragkou, V., Parker, Q. A., Zijlstra, A. A., et al. 2022, *ApJL*, 935, L35, doi: [10.3847/2041-8213/ac88c1](https://doi.org/10.3847/2041-8213/ac88c1)
- Fragkou, V., Vázquez, R., Parker, Q. A., Gonçalves, D. R., & Lomelí-Núñez, L. 2025, *A&A*, 696, A146, doi: [10.1051/0004-6361/202453031](https://doi.org/10.1051/0004-6361/202453031)
- Freudling, W., Romaniello, M., Bramich, D. M., et al. 2013, *A&A*, 559, A96, doi: [10.1051/0004-6361/201322494](https://doi.org/10.1051/0004-6361/201322494)
- Frew, D. J., Bojičić, I. S., & Parker, Q. A. 2013, *MNRAS*, 431, 2, doi: [10.1093/mnras/sts393](https://doi.org/10.1093/mnras/sts393)
- Frew, D. J., Parker, Q. A., & Bojičić, I. S. 2016, *MNRAS*, 455, 1459, doi: [10.1093/mnras/stv1516](https://doi.org/10.1093/mnras/stv1516)
- Gaia Collaboration, Klioner, S. A., Lindegren, L., et al. 2022, *A&A*, 667, A148, doi: [10.1051/0004-6361/202243483](https://doi.org/10.1051/0004-6361/202243483)
- Geller, A. M., Mathieu, R. D., Braden, E. K., et al. 2010, *AJ*, 139, 1383, doi: [10.1088/0004-6256/139/4/1383](https://doi.org/10.1088/0004-6256/139/4/1383)
- Gillett, F. C., Jacoby, G. H., Joyce, R. R., et al. 1989, *ApJ*, 338, 862, doi: [10.1086/167241](https://doi.org/10.1086/167241)
- González-Santamaría, I., Manteiga, M., Manchado, A., et al. 2021, *A&A*, 656, A51, doi: [10.1051/0004-6361/202141916](https://doi.org/10.1051/0004-6361/202141916)
- Hao, C. J., Xu, Y., Wu, Z. Y., et al. 2022, *A&A*, 660, A4, doi: [10.1051/0004-6361/202243091](https://doi.org/10.1051/0004-6361/202243091)
- Hao, C. J., Xu, Y., Hou, L. G., et al. 2021, *A&A*, 652, A102, doi: [10.1051/0004-6361/202140608](https://doi.org/10.1051/0004-6361/202140608)
- Hunt, E. L., & Reffert, S. 2024, *A&A*, 686, A42, doi: [10.1051/0004-6361/202348662](https://doi.org/10.1051/0004-6361/202348662)
- Jacob, R., Schönberner, D., & Steffen, M. 2013, *A&A*, 558, A78, doi: [10.1051/0004-6361/201321532](https://doi.org/10.1051/0004-6361/201321532)
- Jacoby, G. H., De Marco, O., Davies, J., et al. 2017, *ApJ*, 836, 93, doi: [10.3847/1538-4357/836/1/93](https://doi.org/10.3847/1538-4357/836/1/93)
- Jacoby, G. H., Morse, J. A., Fullton, L. K., Kwitter, K. B., & Henry, R. B. C. 1997, *AJ*, 114, 2611, doi: [10.1086/118671](https://doi.org/10.1086/118671)
- Kharchenko, N. V., Piskunov, A. E., Schilbach, E., Röser, S., & Scholz, R. D. 2013, *A&A*, 558, A53, doi: [10.1051/0004-6361/201322302](https://doi.org/10.1051/0004-6361/201322302)
- Kingsburgh, R. L., & Barlow, M. J. 1994, *MNRAS*, 271, 257, doi: [10.1093/mnras/271.2.257](https://doi.org/10.1093/mnras/271.2.257)
- Kniazhev, A. Y., Gvaramadze, V. V., & Berdnikov, L. N. 2016, *MNRAS*, 459, 3068, doi: [10.1093/mnras/stw889](https://doi.org/10.1093/mnras/stw889)
- Kniazhev, A. Y., Gvaramadze, V. V., & Berdnikov, L. N. 2017, in *Astronomical Society of the Pacific Conference Series*, Vol. 510, *Stars: From Collapse to Collapse*, ed. Y. Y. Balega, D. O. Kudryavtsev, I. I. Romanyuk, & I. A. Yakunin, 480, doi: [10.48550/arXiv.1612.00292](https://doi.org/10.48550/arXiv.1612.00292)
- Labrie, K., Simpson, C., Cardenas, R., et al. 2023, *Research Notes of the American Astronomical Society*, 7, 214, doi: [10.3847/2515-5172/ad0044](https://doi.org/10.3847/2515-5172/ad0044)
- Li, Z., Deng, Y., Chi, H., et al. 2022, *ApJS*, 259, 19, doi: [10.3847/1538-4365/ac3c49](https://doi.org/10.3847/1538-4365/ac3c49)
- Liu, D., Xu, Y., Hao, C., et al. 2023, *ApJS*, 268, 46, doi: [10.3847/1538-4365/acf3e3](https://doi.org/10.3847/1538-4365/acf3e3)
- Liu, L., & Pang, X. 2019, *ApJS*, 245, 32, doi: [10.3847/1538-4365/ab530a](https://doi.org/10.3847/1538-4365/ab530a)
- Luridiana, V., Morisset, C., & Shaw, R. A. 2015, *A&A*, 573, A42, doi: [10.1051/0004-6361/201323152](https://doi.org/10.1051/0004-6361/201323152)
- Marigo, P., Girardi, L., Bressan, A., et al. 2017, *ApJ*, 835, 77, doi: [10.3847/1538-4357/835/1/77](https://doi.org/10.3847/1538-4357/835/1/77)
- Miller Bertolami, M. M. 2016, *A&A*, 588, A25, doi: [10.1051/0004-6361/201526577](https://doi.org/10.1051/0004-6361/201526577)

- Monteiro, H., Dias, W. S., Hickel, G. R., & Caetano, T. C. 2017, *NewA*, 51, 15, doi: [10.1016/j.newast.2016.08.001](https://doi.org/10.1016/j.newast.2016.08.001)
- O'Donnell, J. E. 1994, *ApJ*, 422, 158, doi: [10.1086/173713](https://doi.org/10.1086/173713)
- Osterbrock, D. E., & Ferland, G. J. 2006, *Astrophysics of gaseous nebulae and active galactic nuclei*
- Parker, Q. A., Bojičić, I. S., & Frew, D. J. 2016, in *Journal of Physics Conference Series*, Vol. 728, *Journal of Physics Conference Series (IOP)*, 032008, doi: [10.1088/1742-6596/728/3/032008](https://doi.org/10.1088/1742-6596/728/3/032008)
- Parker, Q. A., Frew, D. J., Miszalski, B., et al. 2011, *MNRAS*, 413, 1835, doi: [10.1111/j.1365-2966.2011.18259.x](https://doi.org/10.1111/j.1365-2966.2011.18259.x)
- Parker, Q. A., Xiang, Z., & Ritter, A. 2022, *Galaxies*, 10, 32, doi: [10.3390/galaxies10010032](https://doi.org/10.3390/galaxies10010032)
- Parker, Q. A., Phillipps, S., Pierce, M. J., et al. 2005, *MNRAS*, 362, 689, doi: [10.1111/j.1365-2966.2005.09350.x](https://doi.org/10.1111/j.1365-2966.2005.09350.x)
- Parker, Q. A., Acker, A., Frew, D. J., et al. 2006, *MNRAS*, 373, 79, doi: [10.1111/j.1365-2966.2006.10950.x](https://doi.org/10.1111/j.1365-2966.2006.10950.x)
- Pastorelli, G., Marigo, P., Girardi, L., et al. 2019, *MNRAS*, 485, 5666, doi: [10.1093/mnras/stz725](https://doi.org/10.1093/mnras/stz725)
- Pastorelli, G., Marigo, P., Girardi, L., et al. 2020, *MNRAS*, 498, 3283, doi: [10.1093/mnras/staa2565](https://doi.org/10.1093/mnras/staa2565)
- Pease, F. G. 1928, *PASP*, 40, 342, doi: [10.1086/123857](https://doi.org/10.1086/123857)
- Peimbert, M., & Torres-Peimbert, S. 1983, in *IAU Symposium*, Vol. 103, *Planetary Nebulae*, ed. L. H. Aller, 233–242
- Perren, G. I., Vázquez, R. A., & Piatti, A. E. 2015, *A&A*, 576, A6, doi: [10.1051/0004-6361/201424946](https://doi.org/10.1051/0004-6361/201424946)
- Pickles, A., & Depagne, É. 2010, *PASP*, 122, 1437, doi: [10.1086/657947](https://doi.org/10.1086/657947)
- Sampedro, L., Dias, W. S., Alfaro, E. J., Monteiro, H., & Molino, A. 2017, *MNRAS*, 470, 3937, doi: [10.1093/mnras/stx1485](https://doi.org/10.1093/mnras/stx1485)
- Sánchez, N., Alfaro, E. J., & López-Martínez, F. 2020, *MNRAS*, 495, 2882, doi: [10.1093/mnras/staa1359](https://doi.org/10.1093/mnras/staa1359)
- Seleznev, A. F., Carraro, G., Costa, E., & Loktin, A. V. 2010, *NewA*, 15, 61, doi: [10.1016/j.newast.2009.05.011](https://doi.org/10.1016/j.newast.2009.05.011)
- Soubiran, C., Cantat-Gaudin, T., Romero-Gómez, M., et al. 2018, *A&A*, 619, A155, doi: [10.1051/0004-6361/201834020](https://doi.org/10.1051/0004-6361/201834020)
- STScI Development Team. 2013., *Astrophysics Source Code Library*, record ascl:1303.023
- Tang, J., Bressan, A., Rosenfield, P., et al. 2014, *MNRAS*, 445, 4287, doi: [10.1093/mnras/stu2029](https://doi.org/10.1093/mnras/stu2029)
- Tarricq, Y., Soubiran, C., Casamiquela, L., et al. 2021, *A&A*, 647, A19, doi: [10.1051/0004-6361/202039388](https://doi.org/10.1051/0004-6361/202039388)
- Trumpler, R. J. 1930, *Lick Observatory Bulletin*, 420, 154, doi: [10.5479/ADS/bib/1930LicOB.14.154T](https://doi.org/10.5479/ADS/bib/1930LicOB.14.154T)
- van den Bergh, S., & Hagen, G. L. 1975, *AJ*, 80, 11, doi: [10.1086/111707](https://doi.org/10.1086/111707)
- van Groeningen, M. G. J., Castro-Ginard, A., Brown, A. G. A., Casamiquela, L., & Jordi, C. 2023, *A&A*, 675, A68, doi: [10.1051/0004-6361/202345952](https://doi.org/10.1051/0004-6361/202345952)
- Vázquez, R. 2012, *ApJ*, 751, 116, doi: [10.1088/0004-637X/751/2/116](https://doi.org/10.1088/0004-637X/751/2/116)
- Zanstra, H. 1931, *ZA*, 2, 1